Uncertainty-aware State Estimation for Electrochemical Model-based Fast Charging Control of Lithium-ion Batteries

Florian Ringbeck[a,b,1,*], Marvin Garbade[a,1], Dirk Uwe Sauer[a,b,c,d]

[a] *Chair for Electrochemical Energy Conversion and Storage Systems, Institute for Power Electronics and Electrical Drives (ISEA), RWTH Aachen University, Jägerstrasse 17-19, 52066 Aachen, Germany*
[b] *Jülich Aachen Research Alliance, JARA-Energy, Templergraben 55, 52056 Aachen, Germany*
[c] *Helmholtz Institute Münster (HI MS), IEK 12, Forschungszentrum Jülich, 52425 Jülich, Germany*
[d] *Institute for Power Generation and Storage Systems (PGS), E.ON ERC, RWTH Aachen University, Mathieustrasse 10, 52074 Aachen, Germany*

Abstract

Fast charging capability is considered a critical factor for the widespread adoption of electric vehicles. High charging currents can, however, severely affect battery health due to the danger of metallic lithium deposition on the anode and consequent degradation reactions. The charging speed should therefore be limited with respect to battery temperature, state of charge, and cell design, governing the onset point of lithium plating.

Electrochemical models are a suitable tool providing continuous estimates of the anode potential as the main lithium plating indicator while covering a wide operational range. In this article, we present a novel charging control scheme based on a real-time capable simulation framework with adjustable model resolution. A profound investigation of error sources and modeling uncertainties motivates online state corrections towards a lower bound of the anode potential, which are realized by selective adjustments of the lithium distribution within electrode particles based on the full cell voltage error. Simulations of controlled

[*] Corresponding author. Tel.: +49-241-80-96977 Fax: +49-241-80-92203
Email address: batteries@isea.rwth-aachen.de (Florian Ringbeck)
[1] Equal contribution.

and conventional CC charging profiles indicate the importance of continuously adapting the charging power for different operating conditions. Further, simulated state and parameter distortions as they might result from initialization and parameterization errors show that our estimation strategy can mitigate the risk of unsafe control operations.

Keywords: Battery Management Systems, Electrochemical Models, Battery, Kalman Filter, State Estimation, Fast Charging

---

1. Introduction

The electrification of transport is one of the greatest challenges of this decade. Promoted by international climate protection initiatives, increasing concerns about air quality in urban space and resulting governmental support for an ecological traffic turn, electric vehicles (EVs) have evoked tremendous interest by both industry and academia within the past decade. Even though the absolute percentage of EVs is still very small, their market penetration increased drastically over recent years and many European countries as well as car manufacturers worldwide have announced their goals to completely eliminate combustion engines in passenger cars by 2040 and earlier [1–3].

However, a widespread adoption of electromobility is faced by complex consumer demands, some of which pose contradictory design requirements to battery manufacturers. While range anxiety is still present in the lower price segment, hence shifting the focus to increased energy density designs with thicker active material coatings, fast charging capability is considered another key factor for economic success. Thus, it comes that fast charging technologies, capable of delivering around 80 % of the battery's nominal capacity in much less than one hour, are currently being established as a standard [3]. High charging currents can, however, severely affect battery health and safety due to the danger of metallic lithium deposition on the anode and consequent degradation reactions. The charging speed should therefore be limited with respect to battery temperature, state of charge and cell design, governing the onset point of lithium plating.

Widely established charging protocols such as constant-current constant-voltage (CCCV) or multistage constant-current constant-voltage (MCC) [4] use to follow predetermined current trajectories without considering internal battery states in a continuous manner. Observing these internal states by means of an electrochemical model can, however, provide valuable information for a precise real-time control of charging currents and constitute the basis for next-generation battery management systems. The fidelity of these models is inevitably affected by simplifications of the underlying electrochemical processes and parameter inaccuracies, which motivates the use of an online observer for error-dependent state corrections.

Different state estimation approaches have been presented in literature which can be discriminated by the adjusted states, the state estimation algorithm as well as the applied model simplifications. Moura et al. [5] implemented a state observer for a single particle model (SPM) with electrolyte dynamics and analyzed stability and estimation error. To improve observability, only cathode surface lithiation was estimated with a partial differential equation (PDE) Backstepping observer, while anode surface concentration was corrected accordingly to conserve lithium. This is effectively an adjustment of the battery SOC neglecting further possible error sources. Electrolyte concentration was estimated with an open-loop observer. Algorithm performance was tested with constant current and dynamic discharge profiles.

Sturm et al. [6] presented an extended Kalman filter (EKF) applied on a reduced-order electrochemical model. The adjusted states were average solid concentration, lithium flux in the active material, and electrolyte concentration. Also here, anode states were not estimated but only corrected based on the cathode estimation to improve algorithm robustness. The observer scheme was tested for large offsets in the initial state of charge (SOC) of 35-42 %. Errors of less than 1% were achieved after approximately three minutes. All observed states show good agreement to the true states. Yet, the observer relies on a linearization of the model which can impair model accuracy at the operational limits.

Yin et al. [7] applied the polynomial approximations of Subramanian et al. [8] for solid state diffusion, the residue grouping approach of Smith et al. [9] for electrolyte diffusion, and a linearization of the Bulter-Volmer equation to derive a reduced order model. An EKF was then used to estimate the model's states which serve as a basis for a dynamic charging current control based on side reaction potentials. Lithium plating as a further boundary condition for charging was introduced in a further publication by Song et al. [10]. The filter shows good performance when initialized with an SOC offset of 20 %, but shows instabilities at low SOCs. Charging current was controlled by lookup tables translating internal cell states to maximum charging currents. The Kalman filter was used to estimate derived quantities as current densities instead of lithium concentrations.

All publications mentioned here tested the proposed observers for deviations in SOC. Yet, as laid out later, SOC can be determined with reasonable accuracy with conventional algorithms, while parameter deviations influencing the lithium distribution within each electrode will inevitably occur. Furthermore, reduced order models serve as a basis for the proposed observer schemes limiting model accuracy.

In our work, a fully parameterized variable-order electrochemical model including electrolyte and temperature dynamics is considered for optimal charging control with respect to the prevention of negative anode potentials.

This paper addresses model theory and simulation framework development. A novel, application-oriented state estimation scheme is introduced to ensure both reliable predictions of the battery full cell voltage as well as conservative estimates of the anode potential for a safe control of charging currents. We examine our model with respect to convergence by varying its spatial resolution and analyzing the sensitivity of the presented observer and control scheme on certain parameter changes. Charging under different operating conditions is studied in open-loop simulations in order to assess the importance of dynamic current adaptions. The flexible framework allows an easy adaption of the estimation technique to different model complexities.

In follow-up work, an experimental study based on our novel control scheme will be presented. First, the reference cell parameterization by Ecker et al. [12, 13] will be discussed critically. The C++ simulation model with observer and controller will then be implemented on a real-time capable embedded system and utilized for closed-loop charging control of the real battery cell. Experiments will be conducted where fast charging at low-temperatures is considered and compared to the conventional CCCV charging paradigm, giving special emphasis to the detection of lithium plating.

2. Electrochemical Model

The theoretical foundations of the outlined pseudo-2D (P2D) model go back to the work of Doyle, Fuller, and Newman (Doyle-Fuller-Newman-Model) [11], which has more recently been embedded into a novel structural design in terms of a superimposed equivalent circuit model (ECM) by Schmalstieg [12]. Latter provides a meaningful connection of the underlying transport processes based on the assumed cell structure and allows an efficient calculation of the internal potential distribution.

2.1. Charge Transport

The porous electrode structure (see Figure 1) is taken into account by means of lumped values for its porosity ϵ and tortuosity τ (Newman et al. [13]). This leads to a modification of electrolyte diffusion properties and ionic conductivity according to the Bruggeman correlation ([12]):

$$D_{e,eff}(c_e, T) = D_e(c_e, T) \cdot \frac{\epsilon}{\tau} \tag{1}$$

$$\sigma_{e,eff}(c_e, T) = \sigma_e(c_e, T) \cdot \frac{\epsilon}{\tau} \tag{2}$$

where D_e is the electrolyte diffusion coefficient in free electrolyte and σ_e its ionic conductivity, both of which depend on lithium-ion concentration and

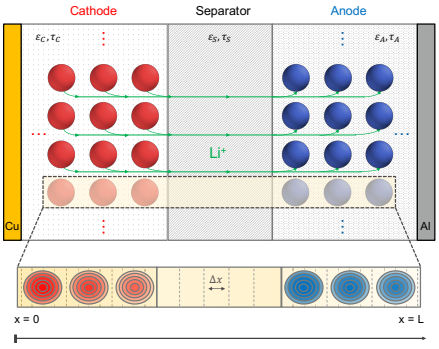

Figure 1: Simplified battery model (P2D model). Lithium-ion movement is modeled by one-dimensional electrolyte diffusion through porous structures in x-direction a well as by spherical diffusion within active material particles (here shown for battery charging). The highlighted extract shows a spatial discretization into volume elements and particle shells.

temperature. This dependency shall be omitted in the following equations for better readability.

In the considered model, electrolyte diffusion is assumed one-dimensional and described by a PDE:

$$\begin{aligned}\frac{\partial c_e(x,t)}{\partial t} =& \frac{1}{\epsilon} \cdot \frac{\partial}{\partial x} \left(D_{e,eff} \cdot \frac{\partial}{\partial x} c_e(x,t) \right) \\ &+ \frac{1}{\epsilon} \cdot \frac{1 - t_0^+}{z \cdot F} \cdot \frac{\partial j_e(x,t)}{\partial x}\end{aligned} \tag{3}$$

where intercalation is described by the pore wall flux $j_{ct} = I_{ct}/A = 1/a \cdot \nabla_x j_e(x,t)$, a is the electrode/electrolyte contact area, F is the Faraday constant, z the charge number ($= 1$ for lithium-ion batteries) and t_0^+ the transference number. The cell dimensions further imply boundary conditions:

$$\left. \frac{\partial c_e(x,t)}{\partial x} \right|_{x=0,L} = 0 \tag{4}$$

where L is the overall distance between opposite current collectors. Further, continuity is imposed at separator/electrode interfaces. Similarly, solid-state diffusion in the active particles can be described by Fick's second law in spherical

coordinates:

$$\frac{\partial c_s(r,t)}{\partial t} = \frac{1}{r^2} \cdot \frac{\partial}{\partial r} \left(D_s \cdot r^2 \cdot \frac{\partial}{\partial r} c_s(r,t) \right) \tag{5}$$

where D_s denotes the particle diffusion coefficient which is also concentration and temperature dependent. Boundary conditions for particle core and surface are given by

$$\left. \frac{\partial c_s(r,t)}{\partial r} \right|_{r=0} = 0 \tag{6}$$

$$\left. \frac{\partial c_s(r,t)}{\partial r} \right|_{r=R_p} = -\frac{1}{D_s} \cdot \frac{I_{ct}}{F \cdot A} \tag{7}$$

where R_p denotes the particle radius and $A = 4\pi R_p^2$ its surface area. Both diffusion processes are coupled by the charge transfer current which can be expressed through the Bulter-Volmer equation:

$$\begin{aligned} I_{ct} = \; & i_0 \cdot A \cdot \left[e^{\frac{\alpha \cdot F}{R \cdot T} \cdot \eta_{ct}} - e^{\frac{(1-\alpha) \cdot F}{R \cdot T} \cdot \eta_{ct}} \right] \\ \underset{\alpha=0.5}{=} \; & 2 \cdot i_0 \cdot A \cdot sinh \left(\frac{F}{2 \cdot R \cdot T} \cdot \eta_{ct} \right) \end{aligned} \tag{8}$$

where i_0 is the exchange current density, η_{ct} the charge transfer overpotential, R the universal gas constant and α the transfer coefficient. Latter can be well approximated by $\alpha = 0.5$. The exchange current density is commonly described by a phenomenological approach [14]:

$$\begin{aligned} i_0 = \; & F \cdot k_0 \cdot (c_{s,max} - c_{ss})^{1-\alpha} \cdot c_{ss}^{\alpha} \cdot c_e^{\alpha} \\ \underset{\alpha=0.5}{=} \; & F \cdot k_0 \cdot \sqrt{(c_{s,max} - c_{ss}) \cdot c_{ss} \cdot c_e} \end{aligned} \tag{9}$$

where c_{ss} denotes the particle surface and $c_{s,max}$ its theoretical maximum concentration.

2.2. Overpotentials

An overpotential due to the internal resistance of electrolyte and solid particles is described by Ohm's law

$$\sigma_i \cdot \frac{\partial \Phi_i}{\partial x} = i_i(x,t) \tag{10}$$

where Φ_i denotes the potential distribution in the electrode or electrolyte, $i_i(x,t)$ the current density and σ_i the respective conductivity. An additional diffusion voltage arises from concentration gradients in the electrolyte:

$$V_{diff} = \frac{R \cdot T}{z \cdot F} \cdot (1 - 2t_0^+) \cdot \frac{\partial ln(c_e)}{\partial x}(x,t) \tag{11}$$

The charge transfer overpotential can be derived from (8) as

$$\eta_{ct} = \frac{2 \cdot R \cdot T}{z \cdot F} \cdot sinh^{-1}\left(\frac{I_{ct}}{2 \cdot i_0 \cdot A}\right) = R_{ct} \cdot I_{ct} \tag{12}$$

where for infinitesimal currents I_{ct} the charge transfer resistance R_{ct} converges to

$$R_{ct} \underset{I_{ct} \to 0}{=} \frac{R \cdot T}{z \cdot F \cdot i_0 \cdot A} \tag{13}$$

As V_{OCV} is measured under resting conditions at a constant electrolyte concentration c_{ref}, an additional concentration overpotential according to Nernst equation has to be incorporated:

$$V_{Nernst} = \frac{R \cdot T}{z \cdot F} \cdot ln\left(\frac{c_e}{c_{e,ref}}\right) \tag{14}$$

These different voltage components can be modeled by means of a superimposed ECM [12] as shown in Figure 2. Every section of the circuit diagram corresponds to a volume element which can either be of type solid, electrolyte or electrode and respectively possesses properties of an electric connection (electrical resistance), ionic connection (ionic resistance, diffusion overpotentials) or the linkage between both transport phases (electrode) comprising all influences of the active material particle and the charge transfer reaction. These volume

elements are interconnected and therefore form a spatial discretization of the cell which can be further refined in terms of additional diffusion elements for a precise approximation of the electrolyte diffusion PDE.

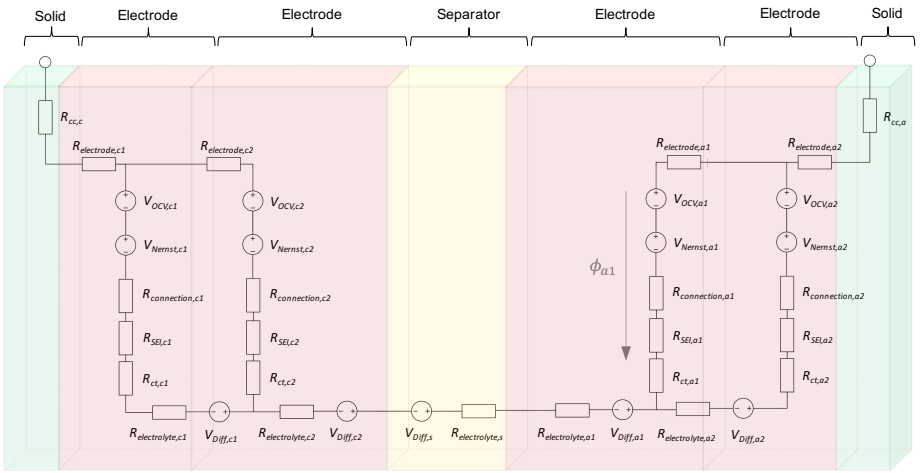

Figure 2: Superimposed electric circuit model (ECM), exemplarily shown for a two-particle model.

The simplest model represents each electrode by a single particle which, in contrast to the original Single Particle Model (SPM), still incorporates electrolyte and temperature dynamics. As the SPM loses precision at high current rates [15], it is reasonable to model several consecutively arranged particles per electrode, each of which forms another parallel branch in the corresponding ECM. Schmalstieg [12] therefore introduced an efficient implicit solution by means of nodal analysis:

$$\boldsymbol{G} \cdot \vec{\Phi} = \vec{I} \tag{15}$$

where the internal potential distribution $\vec{\Phi}$ is determined from the conductance matrix and nodal current vector using Cholesky decomposition.

2.3. Temperature Model

Finally, the influence of temperature is considered through respective parameter dependencies and a lumped thermal model. All diffusion coefficients,

exchange current densities, and the electrolyte conductivity are described according to the Arrhenius equation

$$X = X_{ref} \cdot exp\left(\frac{E_{A,X}}{R} \cdot \left(\frac{1}{T_{ref}} - \frac{1}{T}\right)\right) \tag{16}$$

where the activation energy $E_{A,X}$ can be estimated from multiple measurements at different temperatures.

Schmalstieg [12, 16] developed and validated a lumped thermal model incorporating different heat generation sources:

$$\dot{Q}_{gen} = \dot{Q}_r + \dot{Q}_e + \dot{Q}_p \tag{17}$$

where $\dot{Q}_r$ corresponds to all losses due to electric, ionic or charge transfer resistances (see Figure 2), $\dot{Q}_e$ originates from the electrolyte polarization and $\dot{Q}_p$ from polarization of active material particles. It holds:

$$\dot{Q}_r = (R_e + R_{cc}) \cdot I^2 + (R_{ct} + R_s) \cdot I_{ct}^2 \tag{18}$$

$$\dot{Q}_e = \eta_{diff} \cdot I = \frac{R \cdot T}{z \cdot F} \cdot (1 - 2t_0^+) \cdot \frac{\partial ln(c_e)}{\partial x} \cdot I \tag{19}$$

$$\begin{aligned} \dot{Q}_p = &\left[V_{OCV}(\delta_{surface}) - V_{OCV}(\delta_{average)}\right] \cdot I_{ct} \\ &+ \frac{R \cdot T}{z \cdot F} \cdot ln\left(\frac{c_e}{c_{e,ref}}\right) \cdot I_{ct} \end{aligned} \tag{20}$$

where I is the overall current flowing through current collectors and electrolyte, splitting into different current transfer branches within the electrode, and $\delta_{surface}$, $\delta_{average}$ denote the lithiation of particle surface as well as averaged over the whole particle. The temperature change can be determined with respect to the thermal capacity:

$$\Delta T = \frac{1}{C_{thermal}} \cdot \dot{Q}_{gen} \tag{21}$$

Finally, heat exchange is modeled in two steps from battery bulk to housing and from battery housing to the ambient air by simple heat conduction, given the respective heat conductivity $\lambda_{2\leftrightarrow 1}$ between component 1 and 2:

$$\dot{Q}_{transferred} = \lambda_{2\leftrightarrow 1} \cdot (T_2 - T_1) \tag{22}$$

2.4. Implementation

The described nonlinearly coupled PDEs and ordinary differential equations (ODEs) are transformed into a nonlinear algebraic system according to the Forward Time-Central Space (FTCS) approximation while time updates are performed following Euler's method. For step size Δt and discrete time steps $t = k\Delta t$ with $k = \{0, 1, 2, \dots\}$, it holds:

$$c_i^{k+1} = c_i^k + \Delta t \cdot \frac{\partial c_i^k}{\partial t} \tag{23}$$

The spatial cell division into constituent volume and diffusion elements is shown schematically in Figure 1. Each diffusion element has a homogeneous electrolyte concentration whereby the encapsulating volume element is attributed with their average concentration. Thus, electrolyte diffusion can be modeled with a finer resolution while lithium intercalation into a solid particle is again assumed homogeneous, governed by the mean electrolyte concentration within the surrounding volume element. Electrolyte diffusion (Eq. 3) becomes [12]:

$$\begin{aligned}\frac{\partial c_{e,i}^k}{\partial t} =& \frac{1}{\epsilon_i} \cdot \frac{1}{\Delta x_i} \cdot \\ & \left(\frac{(\epsilon/\tau)_{i+1} + (\epsilon/\tau)_i}{2} \cdot \frac{D_{e,i+1} + D_{e,i}}{2} \cdot \frac{c_{i+1} - c_i}{\frac{\Delta x_{i+1} + \Delta x_i}{2}} \right. \\ & \left. - \frac{(\epsilon/\tau)_i + (\epsilon/\tau)_{i-1}}{2} \cdot \frac{D_{e,i} + D_{e,i-1}}{2} \cdot \frac{c_i - c_{i-1}}{\frac{\Delta x_i + \Delta x_{i-1}}{2}} \right)\end{aligned} \tag{24}$$

The first term of the difference enclosed in parentheses refers to right-sided diffusion whereas the second term refers to left-sided diffusion where index i specifies the diffusion element (all numbered in x-direction) and Δx_i denotes

the diffusion element's width. Similarly, as described by [12], particles are discretized in the spherical domain into shells with identical volume such that the shell thickness decreases with increasing radius.

Shell thickness and mean radius can be derived as

$$\Delta r_i = r_{i,surf} - r_{i-1,surf} \tag{25}$$

$$r_i = r_{i,surf} - \frac{\Delta r_i}{2} \tag{26}$$

which will be the only relevant quantities here. By applying the central difference quotient twice and averaging both diffusion directions in order to ensure lithium conservation ([12]), one can derive the rate of change of solid concentration:

$$\frac{\partial c^k_{s,i\leftrightarrow i+1}}{\partial t} = (D_{s,i+1} + D_{s,i}) \cdot (c_{s,i+1} - c_{s,i}) \cdot X_{i\leftrightarrow i+1} \tag{27}$$

where $X_{i\leftrightarrow i+1}$ is a constant geometry factor extracted from the resulting difference quotient defined as:

$$\begin{aligned} X_{i\leftrightarrow i+1} = \frac{1}{4} \cdot \left(\frac{1}{r_i^2 \cdot \Delta r_i} + \frac{1}{r_{i+1}^2 \cdot \Delta r_{i+1}} \right) \\ \cdot \left(r_i + \frac{\Delta r_i}{2} \right)^2 \cdot \frac{1}{\frac{\Delta r_{i+1} + \Delta r_i}{2}} \end{aligned} \tag{28}$$

Von Neumann stability analysis was employed to determine maximum step sizes with respect to model parameters. Concentration and temperature dependencies must be considered here, such that the maximum step sizes for calculating diffusion processes is obtained by maximizing diffusion coefficients over all possible concentrations and considering a fixed maximum temperature.

3. Estimation & Control

As a basis for subsequent controller and observer design, the model shall be considered in nonlinear state space form where internal states can be regarded

as the battery temperature and the distribution of lithium-ion concentrations across both electrodes and the electrolyte. All of these states have a nonlinear direct (electrolyte and particle surface concentrations) or indirect (particle bulk concentrations and temperature) influence on the output voltage while exhibiting complex interdependencies with the underlying parameter set. The aim of an observer is to update the state vector such that it converges to the true system state when minimizing the output error. The essential question is how the true state can be inferred from available measurements. Therefore, possible reasons for a deviation between model output and the measurement voltage shall be investigated in the following.

3.1. Model Error Investigation

Aiming at physically reasonable state estimates, we observe four causes for unreliable state updates.

- **Measurement Errors**

  Voltage, current and temperature measurements are subject to measurement distortions. This entails errors in SOC estimation by current integration as well as distorted parameter values due to temperature inaccuracies.

- **Parameter Errors**

  Even for advanced experimental setups, some parameters, especially electrochemical cell properties, are very difficult to obtain and exhibit strong variances throughout the literature (see [17]). Constructing half cells for single electrode measurements can induce further errors, e.g. due to structural damages, which are hardly assessable. Moreover, parameter variations among cells (especially among those from different batches) and changes due to battery aging should be mentioned as possible error sources.

- **Model Errors**

  The described model relies on many simplifications that differ from the real

battery cell. Above all, the assumed homogeneous distribution of spherical particles is in contrast to the differently sized particles and electrode inhomogeneities which result in a non-uniform current distribution and locally accelerated aging. Transport processes are solely approximated by Fick's Law and temperature dependencies as well as the charge transfer reactions are based on phenomenological equations that partially exhibit poor agreement with laboratory measurements. Further, the model under investigation excludes several effects such as mechanical stress and volume changes, the electric double layer or the influence of an anode overhang.

- **State Ambiguities**

  Considering a spatial model discretization into N_e diffusion elements for the electrolyte, N_p particles per electrode with M_p particle shells, the overall state vector comprises $N_e + 2N_pM_p$ discrete concentrations which exhibit strong ambiguities for many load profiles. That is, considering the large state space dimension, many different adaptations of the state vector may lead to the same result with respect to the output voltage.

3.2. State Observer Design

The above described flaws of the simulation setup evoke doubts as to the states' physical correctness, which remains questionable under the influence of given inaccuracies. This problem is not limited to our presented model but applies to all existing (P2D-) modeling approaches, many of which are less accurate, e.g. due to neglecting electrolyte or temperature dynamics. The intended charging control scheme, however, relies strongly on trustworthy state estimates in order to prevent negative anode potentials. We therefore seek a cautious estimation strategy where state updates are performed selectively such that the estimated anode potential is never increased by the observer. Further, we consider measurement errors as a result of additive white Gaussian noise (AWGN) with zero mean, whereby the SOC is reliably determined by coulomb counting and battery temperature is obtained through surface-mounted sensors and thus becomes a model input. Latter is likely to result in an underestimation of the

inner battery temperature but avoids a possibly dangerous overestimation due to an inaccurate thermal model which would trigger higher charging currents.

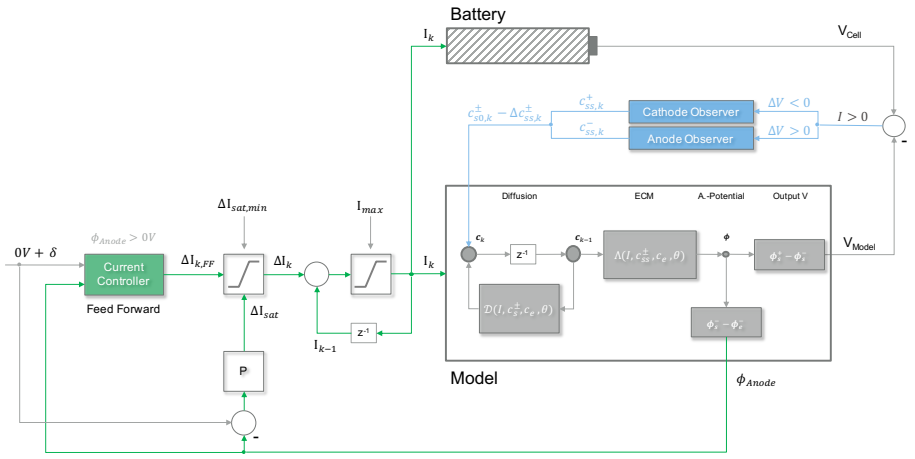

Figure 3: Nonlinear state space representation in closed-loop form. Observer and controller structures are marked in blue and green. The system state corresponds to the distribution of lithium ion concentration within the electrolyte and solid-phase.

Figure 3 shows a state space representation including the observer structure (blue) and control strategy (green). The cell state is described by the distribution of lithium-ion concentrations both within the electrolyte as well as solid-phase and is denoted by c_k for a discrete time step k. States are updated by means of respective diffusion processes, here collectively denoted by $\mathcal{D}$, which corresponds to the system function. The measurement function comprises the calculation of cell potentials by solving the ECM in a first step (denoted by Λ), from which in a second step the cell voltage is obtained by the difference of cathode and anode terminal potentials. Note that Λ is implemented by an implicit computation scheme where the linear system of equations (15) is solved using Cholesky decomposition. Also, note that the diffusion process depends on the whole state vector whereas particle bulk concentrations have no effect on resulting potentials. In order to improve observability, we consider only the surface concentrations of single electrodes for each state update while other system components are simulated open-loop. A single electrode is observed by

means of an unscented Kalman filter (UKF) which performs well for nonlinear systems and can furthermore handle implicit system representations due to the underlying sigma point sampling strategy. Unlike in the original UKF definition [18], zero-mean AWGN on the system states (particle surface concentrations) and measurements (voltage) is assumed in the following.

Let c_{k-1} be the vector of surface concentrations of all particles in the considered electrode at time step $k-1$, $\mathcal{D}_{k|k-1}$ the solid diffusion equation for time step k, based on the previous concentration state as well as input current and temperature I_k and T_k, q_k the system noise vector, $\mathcal{H}_k$ the complete measurement function (including open-loop simulated influences of the electrolyte and opposite electrode), r_k the measurement noise and V_k the resulting battery voltage. The system can then be expressed as

$$c_k = \mathcal{D}_{k|k-1}(c_{k-1}, I_k, T_k) + q_k \tag{29}$$

$$V_k = \mathcal{H}_k(c_k, I_k, T_k) + r_k \tag{30}$$

$$q_k \sim \mathcal{N}(0,\, \boldsymbol{Q}) \quad and \quad r_k \sim \mathcal{N}(0,\, \sigma_r^2) \tag{31}$$

where $\boldsymbol{Q}$ is the system noise covariance matrix and σ_r^2 the measurement noise variance both of which are assumed constant over time. While σ_r can be obtained from the given accuracy of measurement equipment, $\boldsymbol{Q}$ is used to adjust filter dynamics such that a higher system variance leads to faster state updates. Also, a positive correlation of system states (i.e. electrode particle surface concentrations) can be considered herein.

The UKF is initialized according to the current model state and system noise covariance matrix:

$$\hat{c}_0 = \mathbb{E}\left[c_0\right] := c_{ss}^0 \tag{32}$$

$$\boldsymbol{P_0} = \mathbb{E}\left[(c_0 - \hat{c}_0)(c_0 - \hat{c}_0)^T\right] := \boldsymbol{Q} \tag{33}$$

Corresponding UKF equations are stated below.

1. Sigma Point Sampling

$$\begin{aligned}
(\boldsymbol{\mathcal{X}}_{k-1})_0 &= \hat{c}_{k-1|k-1} \\
(\boldsymbol{\mathcal{X}}_{k-1})_i &= \hat{c}_{k-1|k-1} + \left(\sqrt{(N+\lambda)\boldsymbol{P}_{k-1|k-1}}\right)_i, \\
(\boldsymbol{\mathcal{X}}_{k-1})_j &= \hat{c}_{k-1|k-1} - \left(\sqrt{(N+\lambda)\boldsymbol{P}_{k-1|k-1}}\right)_j \\
i &= 0, \ldots, N-1, \quad j = N, \ldots, 2N-1
\end{aligned} \tag{34}$$

with posterior mean and covariance:

$$\begin{aligned}
\hat{c}_{k-1|k-1} &= \sum_{i=0}^{2N-1} W_i \cdot (\boldsymbol{\mathcal{X}}_{k-1})_i \\
\boldsymbol{P}_{k-1|k-1} &= \sum_{i=0}^{2N-1} W_i \cdot \left[(\boldsymbol{\mathcal{X}}_{k-1})_i - \hat{c}_{k-1|k-1}\right] \\
&\qquad \cdot \left[(\boldsymbol{\mathcal{X}}_{k-1})_i - \hat{c}_{k-1|k-1}\right]^T
\end{aligned} \tag{35}$$

and weights W_i:

$$W_0 = \frac{\lambda}{N+\lambda} \quad W_i = \frac{1}{2(N+\lambda)} \quad i \in [1, 2N-1] \tag{36}$$

2. Time Update

$$\boldsymbol{\mathcal{X}}_{k|k-1} = \mathcal{D}_{k|k-1}(\boldsymbol{\mathcal{X}}_{k-1}, I_k, T_k)$$

$$\begin{aligned}
\hat{c}_{k|k-1} &= \sum_{i=0}^{2N-1} W_i \cdot (\boldsymbol{\mathcal{X}}_{k|k-1})_i \\
\boldsymbol{P}_{k|k-1} &= \sum_{i=0}^{2N-1} W_i \cdot \left[(\boldsymbol{\mathcal{X}}_{k|k-1})_i - \hat{c}_{k|k-1}\right] \\
&\qquad \cdot \left[(\boldsymbol{\mathcal{X}}_{k|k-1})_i - \hat{c}_{k|k-1}\right]^T + \boldsymbol{Q}
\end{aligned} \tag{37}$$

with estimated output voltage:

$$\mathcal{V}_{k|k-1} = \mathcal{H}_k(\boldsymbol{\mathcal{X}}_{k|k-1}, I_k, T_k)$$

$$\hat{V}_{k|k-1} = \sum_{i=0}^{2N-1} W_i \cdot (\mathcal{V}_{k|k-1})_i \tag{38}$$

3. Kalman Gain Computation

$$
\begin{aligned}
P_{V_k V_k} = & \sum_{i=0}^{2N-1} W_i \cdot \left[(\mathcal{V}_{k|k-1})_i - \hat{V}_{k|k-1} \right] \\
& \cdot \left[(\mathcal{V}_{k|k-1})_i - \hat{V}_{k|k-1} \right]^T + \sigma_r^2 \\
P_{c_k V_k} = & \sum_{i=0}^{2N-1} W_i \cdot \left[(\boldsymbol{\mathcal{X}}_{k|k-1})_i - \hat{c}_{k|k-1} \right] \\
& \cdot \left[(\mathcal{V}_{k|k-1})_i - \hat{V}_{k|k-1} \right]^T \\
\mathcal{K}_k = & P_{c_k V_k} P_{V_k V_k}^{-1}
\end{aligned}
\tag{39}
$$

4. Measurement Update

$$
\begin{aligned}
\hat{c}_{k|k} &= \hat{c}_{k|k-1} + \mathcal{K}_k \cdot (V_k - \hat{V}_{k|k-1}) \\
\boldsymbol{P}_{k|k} &= \boldsymbol{P}_{k|k-1} - \mathcal{K}_k P_{V_k V_k} \mathcal{K}_k^T
\end{aligned}
\tag{40}
$$

At each iteration, sigma points $\boldsymbol{\mathcal{X}}$ are sampled around the current state estimate with a spread according to the current state covariance matrix and a scaling parameter λ, which comprises additional parameters tweaking the shape of the desired Gaussian in case of additional prior knowledge regarding the state distribution but has been empirically adjusted to a fixed value of $\lambda = 2$ here.

The presented single electrode observer is already capable of adjusting particle surface concentrations of one selected electrode such that simulated and measured output voltage coincide. Due to the low gradient of the anode OCV, a cathode observer generally performs better though, however, only adjustments of anode states have an influence on the control-relevant anode potential.

In order to achieve the aforementioned decrease of anode potential, two single electrode observers for both electrodes are assembled to a superordinate observer which performs a case discrimination before each update step. As both electrode OCVs are monotonically decreasing with particle surface SOC, an update of anode surface concentrations shall take place if the simulated voltage

lies below the measurement, resulting in a decreased anode potential [2], while for too large simulation outputs, cathode surface concentrations shall be adapted. This always results in an increase of surface concentrations in both electrodes. By evaluating the sign of voltage error, the superordinate observer always selects the appropriate single electrode observer for state adjustment while the opposite estimator is reset to its initial state. Due to the assumed correct SOC, lithium balance is preserved by subtracting excess lithium generated on the particle surface only from the particle core, so that the concentration gradient within the particle is effectively raised. This correction consequently provokes accelerated diffusion, which should hereby automatically reverse the lithium reallocation made by the observer over time.

3.3. Charging Control

Charging control aims to keep the anode potential at a given safety offset $\delta > 0\,V$. The anode potential is directly influenced by the input current in terms of resulting charge transfer and ohmic overpotentials and further changes over time due to lithium intercalation. During battery charging, lithium is moved from cathode to anode where particles at the electrode-separator interface are lithiated faster due to the tortuous electrode structure. Therefore, lithium plating is likely to first occur at inner particles surfaces, which should hence be considered for current control. Referring to the corresponding ECM (Figure 2), the anode potential is given by

$$\begin{aligned}\Phi_{a1} =& I_{ct,a1} \cdot (R_{ct,a1} + R_{connection,a1} + R_{SEI,a1}) \\ &+ V_{OCV,a1} + V_{Nernst,a1}\end{aligned} \tag{41}$$

where $I_{ct,a1}$ is the exchange current in the inner anode branch and is defined negative for intercalation.

A simple but efficient stepwise feedforward control scheme has been employed in

[2] A temporal increase of the anode potential due to nonlinear charge transfer characteristics (see. Eq. 9) would be quickly corrected in subsequent estimation steps.

this work, based on the assumption of current-independent ECM components, i.e. the amount of transferred lithium is assumed ineffectively low between two successive control operations and the current dependency of R_{ct} (Eq. (12)) becomes negligible for small changes ΔI of the input current. An adjustment of the input current would hence induce a proportional change of exchange currents in all electrode branches. Summarizing all branch resistances at time step k as R_{a1}, the change of input current can thereby be determined as:

$$\Delta I_{k,FF} = I_{k-1} \left(\frac{\delta - (V_{OCV,a1} + V_{Nernst,a1})}{R_{a1} \cdot (I_{ct,a1})_{k-1}} - 1 \right) \tag{42}$$

As the above assumption only holds for sufficiently small current changes, it is reasonable to limit the step size. In order to increase control dynamics for large error terms, current steps are saturated with a maximum step size $\Delta I_{sat,max}$ that is calculated by a P-controller until a defined minimum $\Delta I_{sat,min}$ is reached. It holds:

$$\Delta I_{sat,max} = \max \left\{ P \cdot (\delta - \Phi_{a1}),\ \Delta I_{sat,min} \right\} \tag{43}$$

$$\Delta I_k = \min \left\{ \Delta I_{k,FF},\ \Delta I_{sat,max} \right\} \tag{44}$$

Both parameters P and $\Delta I_{sat,min}$ are set empirically, aiming at dynamic control behavior with minimized overshoot. The new input current is then set according to

$$I_k = \max \left\{ I_{k-1} + \Delta I_k,\ I_{max} \right\} \tag{45}$$

where I_{max} is the overall current limit of the charging device. Following this approach, multiple tests with a rather slow update frequency of 1 Hz have shown a robust control behavior where the desired setpoint was reached within a few seconds.

4. Reference Model

To demonstrate the benefits of our proposed state observer and control scheme, a simulative investigation was done. The model configuration used for subsequent simulations is presented in the following sections.

4.1. Model Parameterization

All simulations were conducted based on the parameters of a commercially available 7.5 A h pouch cell (Kokam SLPB 75106100), for which a full parameter set had been obtained and validated experimentally in previous work [17, 19]. Active material diffusion was here characterized by GITT measurements, which we implemented according to the improved analysis method for GITT data presented in [20]. This results in a less volatile diffusion coefficient over SOC, which is physically more reasonable and also improves model robustness. The according analysis and resulting diffusion coefficient is presented in Appendix A.

Furthermore, following common model order reductions, the transfer coefficients α of anode and cathode are assumed to be 0.5.

Apart from the referenced parameter set, additional parameters for the thermal model according to section 2.3 must be determined.

Heat capacity of the bulk was measured to be $165\,\mathrm{J\,K^{-1}}$ based on the method presented in [21]. Cell case capacity was assumed to be $1\,\mathrm{J\,K^{-1}}$.

We assume a lumped generation of all losses at the center of the cell, so that a specific heat conductivity of $0.5\,\mathrm{W\,m^{-1}\,K^{-1}}$ leads to a thermal conductivity of $2.15\,\mathrm{W\,K^{-1}}$ between heat generation and case. The assumed specific thermal conductivity is based on [22–25].

Assuming natural convection on a vertical plate, an ambient temperature of $-5\,^{\circ}\mathrm{C}$ and a constant cell surface temperature of approximately $10\,^{\circ}\mathrm{C}$, the thermal conductivity between case and ambient is $0.1164\,\mathrm{W\,K^{-1}}$. The cell surface temperature serves as a worst-case assumption as a high surface temperature improves convective cooling and therefore inhibits bulk self-heating. The deriva-

tion of the thermal dissipation by convective heating is depicted in Appendix A. The complete parameter set used for simulation is depicted in table A.2.

4.2. Model Discretization

As described in section 2.4 solid and electrolyte domains are discretized and according ODEs are derived. A fixed step solver is then applied on the ODEs, allowing for a constant execution time in a realtime environment.

A coarser discretization in each domain leads to less computational burden but an increased simulation error. While in a non-realtime application, the discretization would be refined until convergence of the predicted quantities is reached, the ideal discretization grid for an online application can be coarser and is a compromise between accuracy and computational speed, which depends on cell parameters as well as expected temperatures and load currents.

To identify a proper discretization, an analysis of the computational error and performance was conducted. For this, we simulated a 20 A constant current charge from 2.7 V to 4.2 V with different discretization in x- and r-domain. The chosen discretization steps were between 6 to 120 shells in r-direction and 1 to 6 particles with three electrolyte volume elements per particle for x-direction. Particle count was kept constant at one particle per electrode for the analysis of particle discretization. For the analysis in x-direction, particle discretization was held constant at 120 shells. The simulation was isothermal at 5 °C, as we wanted to especially focus on low-temperature behavior of the battery cell during charging. Neglecting the self-heating serves as a worst-case, since diffusion coefficients decrease with temperature resulting in increased errors for coarse discretizations. The results of these simulations are depicted in figure 4. Variation over particle discretization is depicted in the left column and shows significant accuracy gains between 6 and 60 shells. While calculation time is increased by a factor of approximately 6, the simulation error is decreased from 35 mV to 2 mV. Furthermore, also the voltage curve form of the 6 shell model deviates from the other trajectories, highlighting the inaccuracies caused by an overly coarse discretization.

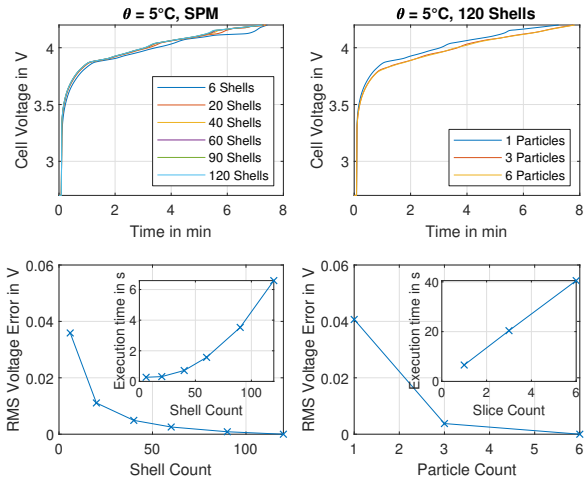

Figure 4: Model error for different discretizations for a 20 A constant current charge at 5 °C. Top Left: Full cell voltage of a single particle model with electrolyte dynamics with different particle discretizations (shells). Bottom Left: RMS error of full cell voltage and execution time with respect to the 120 shell solution. Top Right: Full cell voltage of model with different particle count and electrolyte discretizations. Bottom Right: RMS error of full cell voltage and execution time with respect to the 6 particle model.

Particle count variation results are depicted in the right column. An offset between the single particle model from the finer discretizations can be observed. An increase in particle count from 1 to 3 decreases the voltage error by approximately 35 mV but increases the calculation time of the model by a factor of 3. Based on these results, a discretization with 60 shells in r-direction is chosen for the further simulations. Even though an SPM with electrolyte dynamics leads to small inaccuracies, we choose a discretization of one particle per electrode in x-direction, as the computational burden is drastically decreased and the resulting error can be mitigated by keeping a safety margin during current control.

5. Charging Control

To quantify the benefits of plating side reaction potential controlled charging, we conducted several simulations where conventional constant current charging

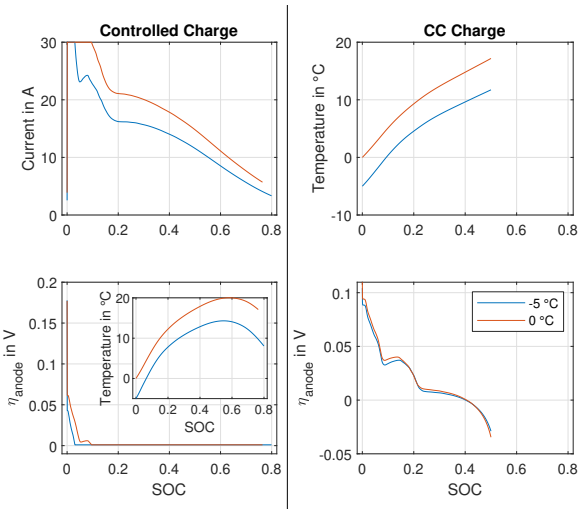

Figure 5: Comparison of anode voltage controlled charging and CC charging at −5 °C and 0 °C. Left column: Controlled charging. Right column: CC charging with average C-Rate of the according controlled charge. Both simulations were stopped at the beginning of the CV-phase.

is taken as a benchmark. To reduce the influence of discretization errors, the model is discretized with three particles per electrode and 60 shells per particle for this analysis.

As plating is likely to occur at low temperatures, we analyze the cell performance at ambient temperatures of 0 °C and −5 °C. According to the data sheet, charging is prohibited below 0 °C, indicating the danger of plating in this temperature range. Charging is started at an SOC of 10 % and stopped at an SOC of 80 % or the beginning of lithium plating. The setpoint of the anode voltage controller is fixed to 1 mV.

The simulation results are depicted in figure 5. The left column shows current, anode potential and temperature for controlled charging while the right column depicts the results for CC-charging. The current of the CC-charging scheme was set to the average current of the controlled charging simulations, which is approximately 2.1 C at 0 °C and 1.7 C at −5 °C, resulting in similar charging overall times. This charging speed is also above the specified 2 C which are

allowed above 0 °C. An SOC of 80 % was reached after 22 and 29 minutes respectively. Controlled charging current was limited to 30 A.

The controlled current trajectories exhibit a characteristic shape where initial high current peaks are followed by an exponential decrease in the course of ongoing particle surface lithiation. Utilizing the initially higher charge acceptance results in a considerable temperature rise due to ohmic losses that again contributes to enhanced charging capability, constituting an essential synergy effect of this approach. At higher temperatures, i_0 and D_s are increased due to their Arrhenius temperature dependency, so that overpotentials are effectively lowered. Temperature decreases later on, when the current is lowered due to anode side reaction potential limitations. The temperature increase is in line with [26] who measured a temperature increase to 23 °C when charging with 4 C at 0 °C ambient temperature for the same cell.

In contrast to this, the CC-Profile shows a lower peak temperature but no cool down in the course of the charge. According to the intended side reaction potential limitation, charging currents are too high from approximately 40 to 50 % SOC onwards, so that lithium plating is expected to occur.

6. State Observer Performance

To characterize the performance of the proposed observer, we assessed the filter response in the presence of different error sources as previously described. In total, three models were simulated. One reference model representing the measured cell, a distorted open-loop model without state correction and the closed-loop model with state feedback. Using a simulation model as reference, different error sources can be evaluated also with respect to the true internal battery states.

The proposed observer was compared to a single electrode observer, which only adapts the cathode surface concentration. The battery cells were charged with a 1 C current rate from 10 % SOC to 4.2 V with no subsequent CV-phase. The

simulations were conducted isothermally at a temperature of −5 °C. The closed- and open-loop models were then altered in different ways to reflect possible error scenarios:

- **Modification of D_s^-**

  The determination of diffusion coefficients in coin cell measurements is influenced by several possible error sources. For instance, the production of coin cells may change the properties of the active material. Furthermore, GITT measurements used to determine the diffusion coefficient rely on simplifications of the actual cell behavior. Additionally, many other publications assume the diffusion coefficient to be independent of active material lithiation, possibly leading to parameter errors in an order of magnitude for some SOCs. Besides, inaccurate temperature estimations can lead to large variations in this parameter due to its Arrhenius dependency. The anode diffusion coefficient varies by roughly one order of magnitude between −20 °C and 50 °C.

  Therefore, we altered the solid state diffusion coefficient D_s^- of the anode to assess the impact of these errors on state estimation. We chose three fixed values with the minimum, the maximum and a mean value of the coefficient as presented in [17].

- **Modification of i_0^-**

  The determination of the anode exchange current density is subject to similar error sources as the diffusion parameter measurement. Also here, coin cells are built for parameter determination. Furthermore, a subsequent impedance fitting process is used, adding further inaccuracies. This is also reflected by the original publication on the used parameter set [17, 19], where i_0 was subsequently changed significantly from the parameters determined by coin cell measurements in order to improve agreement between full cell model and measurement.

  The temperature dependency is stronger for this parameter than for the

diffusion coefficient leading to variations of roughly three decades between $-20\,°C$ and $50\,°C$.

We scale the exchange current density of the closed and open-loop model by one decade in both directions.

- **Offset in initial electrode lithiation**

  Due to wrong initial parameterization or cell aging, the initial lithiation of one electrode might change. For example, the loss of lithium inventory (LLI) leads to a shift in the initial lithiation of anode and cathode. Four scenarios were considered here, each with an increase or decrease of closed- and open-loop model cathode and anode initial lithiations.

- **Offset in initial SOC**

  Due to voltage measurement errors, the initial SOC of the cell might also be offset. To simulate this error, a change in estimator model full cell initial SOC of $5\,\%$ in positive and negative direction was conducted.

- **Single Particle Model**

  The here used single particle model with electrolyte dynamics already poses a model order reduction and therefore an error source. As a model with more particles per electrode reflects the actual battery behavior more precisely, we also conducted simulations with a model comprising three particles per electrode as a reference model. For this multiple particle reference, the particle closest to the separator was compared to the single particle of the controller model.

An overview of the parameter modifications is also given in table 1.

To evaluate the estimator performance in each scenario, we define three error metrics. The quality of the full cell voltage as a result of state corrections is evaluated by the root mean square (RMS) error with respect to the reference model cell voltage. Equally, the anode potential estimation error is evaluated by RMS error. In order to get a more application-oriented error metric penalizing overestimated anode potentials that could result in harmful control operations,

Symbol	Description
$D_s^- = 10^{-10}$	Anode diffusion coefficient fixed to $10 \times 10^{-10}\,\mathrm{cm}^2\,\mathrm{s}^{-1}$
$D_s^- = 10^{-8.5}$	Anode diffusion coefficient fixed to $10 \times 10^{-8.5}\,\mathrm{cm}^2\,\mathrm{s}^{-1}$
$D_s^- = 10^{-11}$	Anode diffusion coefficient fixed to $10 \times 10^{-11}\,\mathrm{cm}^2\,\mathrm{s}^{-1}$
SOC^-_{-10}	Initial anode SOC reduced by 10 %
SOC^-_{+10}	Initial anode SOC raised by 10 %
SOC^+_{-10}	Initial cathode SOC reduced by 10 %
SOC^+_{+10}	Initial cathode SOC raised by 10 %
SOC_{-5}	Initial full cell SOC reduced by 5 %
SOC_{+20}	Initial full cell SOC raised by 20 %
$i_0^- = 0.1 \cdot i_{0,ref}^-$	Anode exchange current density reduced by a factor of 10.
$i_0^- = 10 \cdot i_{0,ref}^-$	Anode exchange current density increased by a factor of 10.
Mutliple Particles	3 particles per electrode in reference model

Table 1: Model parameter variations for observer benchmarking.

we also compute the normalized positive error surface

$$V_{anode,err,surf} = \frac{1}{N} \sum_{i=0}^{N} V_{anode,err,i} \quad \text{where } V_{anode,err,i} > 0 \tag{46}$$

with $V_{anode,err} = V_{anode,cl} - V_{anode,ref}$. Consequently, $V_{anode,err,i} > 0$ indicates an overestimation of the anode potential.

6.1. Single Electrode Cathode Observer

Due to the higher cathode OCV gradient and resulting superior performance compared to an anode single electrode observer, a cathode observer serves as a reference for the evaluation of the newly proposed observer scheme. Model parameters and discretization for the following simulations were chosen according to section 4.2. The above-described parameter variations were applied on the observer model, which was then run with an unmodified model as a reference.

Exemplarily, results of a simulation with a fixed D_s^- to the mean value of $1 \times 10^{-10}\,\mathrm{cm}^2\,\mathrm{s}^{-1}$ are depicted in figure 6.

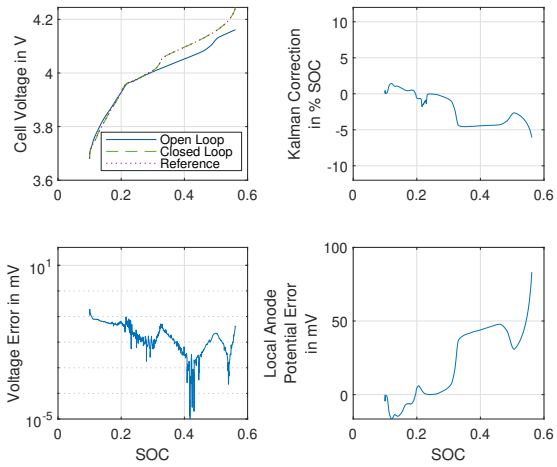

Figure 6: Cathode Observer. Simulation of a 1C charge of a battery cell with a closed-loop and open-loop model with altered D_s^-. Top left: reference voltage (dotted line), closed-loop voltage (dashed line), open-loop voltage (solid line). Bottom left: logarithmic voltage error $V_{cl} - V_{ref}$. Top right: correction of surface SOC. Bottom right: anode potential error $V_{anode,cl} - V_{anode,ref}$.

As shown in the bottom left plot, the voltage error between the closed-loop model and the reference model is kept well below 1 mV by the Kalman filter. Yet, as the cathode surface concentration is corrected to compensate for an anode parameter error, this compensation is not physically correct. This becomes apparent when comparing the estimated anode potential to the true anode potential as in the bottom right plot of figure 6. Compared to the reference model, the error is in the range of 10 mV to 60 mV . When applying this observer in combination with a fast charging controller, the actual anode potential is overestimated, possibly leading to dangerously high charging currents.

Figure 8 depicts the results of all simulation scenarios and compares these to the later discussed novel observer based on RMS and positive anode potential error surface.

For all scenarios, the RMS error of the full cell voltage estimation is below 1 mV again proving the good performance of the Kalman filter.

The same application-relevant overestimation of the anode potential as in

the case of $D_s^- = 10 \times 10^{-10}\,\mathrm{cm^2\,s^{-1}}$ can be observed for several other scenarios, as for example an altered anode SOC, an offset in full cell SOC or an overestimated exchange current density.

A normalized positive error surface of 0 does not necessarily indicate a correct anode potential estimation but could also imply an underestimation of the anode potential, which would, however, only lead to reduced and hence safe charging currents. Yet, for the cathode state deviations, the anode potential is correctly estimated.

Summarizing, we have shown that a successful adoption of the full cell battery voltage through a state observer does not always result in physically meaningful model states, given the aforementioned ambiguities due to different superimposed error sources. If the cause of a compensated error deviates from the compensation mechanism of the estimator, full cell voltage might agree while internal quantities show significant error. An online detection of these cases is challenging as other metrics like the Kalman gain or the trajectory of the full cell voltage error over time might have to be analyzed.

6.2. Proposed Observer

Due to the challenging localization of voltage error sources in order to determine physically correct states, we propose a novel observer as an application-oriented estimation strategy.

The same parameter and state variations as for the cathode observer were conducted for the proposed observer. The results for $D_s^- = 10 \times 10^{-10}\,\mathrm{cm^2\,s^{-1}}$ are depicted in figure 7. Compared to figure 6, the proposed observer reduces the normalized positive error surface by a factor of three. Still, at the end of discharge the filter cannot limit the anode potential error anymore resulting in a positive anode voltage error.

Figure 8 presents the errors for both estimators in comparison. An improvement of the positive anode error surface can be observed for all scenarios affected by such an error except for the multiple particle case. This comes at the cost of an

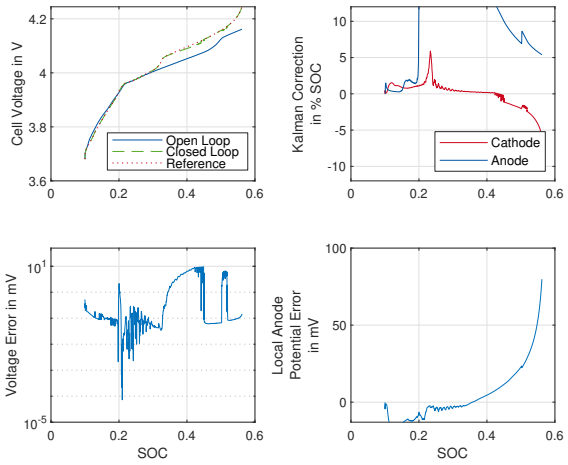

Figure 7: Proposed full cell observer. Simulation of a 1C charge of a battery cell with a closed-loop and open-loop model with altered D_s^-. Top left: reference voltage (yellow), closed-loop voltage (red), open-loop voltage (blue). Bottom left: logarithmic voltage error $V_{cl} - V_{ref}$. Top right: correction of anode and cathode surface SOC. Bottom right: anode potential error $V_{anode,cl} - V_{anode,ref}$.

increased full cell RMS voltage error as well as an increased anode RMS voltage error in some cases.

7. Conclusion

In this paper, we presented a novel state estimation and continuous charging control scheme to prevent lithium plating based on a full-order electrochemical model including relevant temperature- and concentration-dependencies. The C++ implementation allows a flexible adjustment of model resolution and is optimized for real-time capable BMS-integration. Different superimposed error sources for a potential model mismatch were investigated, highlighting the uncertainty in online state and parameter corrections. Hence, a new state observer was developed that selectively adjusts solid particle concentration gradients of anode and cathode, aimed at giving a lower bound of the control-relevant anode potential. By simulating different model distortions and initialization errors it was shown that our proposed estimation scheme can decrease the risk of unsafe

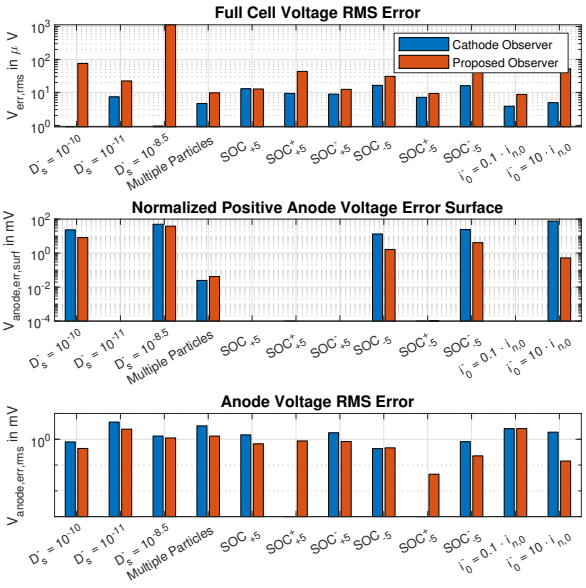

Figure 8: Comparison of full cell and anode voltage errors of cathode observer and proposed observer.

control actions while still accurately following the full-cell voltage. Yet, simulations of high parameter errors as they might occur in measurements of some kinetic cell properties show that undesirable model prediction errors can still not be entirely excluded. In upcoming work, we will closely review the presented experimental cell parameterization and test cells of the same type to investigate closed-loop behavior of our proposed algorithm with respect to charging time, computational performance and aging effects. Future work may focus on a profound examination of model parameter sensitivities, improvements of cell parameterization as well as improved model validation strategies. Further, the effect of battery aging on model accuracy could be studied and included for online parameter adaptations.

Acknowledgements

This work has received funding from the European Unions Horizon 2020 research and innovation program under the grant "Electric Vehicle Enhanced

Range, Lifetime And Safety Through INGenious battery management" (EVERLASTING 713771). The authors would like to thank Dr. Johannes Schmalstieg for the development of the initial model code. The underlying data of this article is available under doi:10.4121/uuid:30a44cee-f94e-466d-a2e0-6239d5fa6bbb.

References

[1] M. Li, J. Lu, Z. Chen, K. Amine, 30 years of lithium-ion batteries, Advanced materials (Deerfield Beach, Fla.) (2018) e1800561doi:10.1002/adma.201800561.

[2] D. V. Pelegov, J. Pontes, Main drivers of battery industry changes: Electric vehicles—a market overview, Batteries 4 (4). doi:10.3390/batteries4040065.
URL http://www.mdpi.com/2313-0105/4/4/65

[3] Ghassan Zubi, Rodolfo Dufo-López, Monica Carvalho, Guzay Pasaoglu, The lithium-ion battery: State of the art and future perspectives, Renewable and Sustainable Energy Reviews 89 (2018) 292–308. doi:10.1016/j.rser.2018.03.002.
URL http://www.sciencedirect.com/science/article/pii/S1364032118300728

[4] Weixiang Shen, Thanh Tu Vo, A. Kapoor, Charging algorithms of lithium-ion batteries: An overview, in: 2012 7th IEEE Conference on Industrial Electronics and Applications (ICIEA), 2012, pp. 1567–1572. doi:10.1109/ICIEA.2012.6360973.

[5] S. J. Moura, F. B. Argomedo, R. Klein, A. Mirtabatabaei, M. Krstic, Battery state estimation for a single particle model with electrolyte dynamics, IEEE Transactions on Control Systems Technology 25 (2) (2017) 453–468. doi:10.1109/TCST.2016.2571663.

[6] J. Sturm, H. Ennifar, S. V. Erhard, A. Rheinfeld, S. Kosch, A. Jossen, State estimation of lithium-ion cells using a physicochemical model based

extended kalman filter, Applied Energy 223 (2018) 103–123. doi:10.1016/j.apenergy.2018.04.011.

[7] Y. Yin, Y. Hu, S.-Y. Choe, H. Cho, W. T. Joe, New fast charging method of lithium-ion batteries based on a reduced order electrochemical model considering side reaction, Journal of Power Sources 423 (2019) 367–379. doi:10.1016/j.jpowsour.2019.03.007.

[8] V. R. Subramanian, V. D. Diwakar, D. Tapriyal, Efficient macro-micro scale coupled modeling of batteries, Journal of The Electrochemical Society 152 (10) (2005) A2002. doi:10.1149/1.2032427.

[9] K. A. Smith, C. D. Rahn, C.-Y. Wang, Control oriented 1d electrochemical model of lithium ion battery, Energy Conversion and Management 48 (9) (2007) 2565–2578. doi:10.1016/j.enconman.2007.03.015.

[10] M. Song, S.-Y. Choe, Fast and safe charging method suppressing side reaction and lithium deposition reaction in lithium ion battery, Journal of Power Sources 436 (2019) 226835. doi:10.1016/j.jpowsour.2019.226835.

[11] M. Doyle, T. F. Fuller, J. Newman, Modeling of galvanostatic charge and discharge of the lithium/polymer/insertion cell, Journal of The Electrochemical Society 140 (6) (1993) 1526. doi:10.1149/1.2221597.

[12] J. Schmalstieg, Physico-electrochemical simulation of lithium-ion batteries : implementation, parametrization and applicationdoi:10.18154/RWTH-2017-04693.

[13] J. Newman, W. Tiedemann, Porous-electrode theory with battery applications, AIChE Journal 21 (1975) 25–41. doi:10.1002/aic.690210103.

[14] W. van Schalkwijk, B. Scrosati, Advances in Lithium-Ion Batteries, Springer, 2002.

[15] A. M. Bizeray, S. Zhao, S. R. Duncan, D. A. Howey, Lithium-ion battery thermal-electrochemical model-based state estimation using orthogonal col-

location and a modified extended kalman filter, Journal of Power Sources 296 (2015) 400–412. doi:10.1016/j.jpowsour.2015.07.019.

[16] J. Schmalstieg, D. U. Sauer, Full cell parameterization of a high-power lithium-ion battery for a physico-chemical model: Part ii. thermal parameters and validation, Journal of The Electrochemical Society 165 (16) (2018) A3811–A3819. doi:10.1149/2.0331816jes.

[17] M. Ecker, T. K. D. Tran, P. Dechent, S. Käbitz, A. Warnecke, D. U. Sauer, Parameterization of a physico-chemical model of a lithium-ion battery: I. determination of parameters, Journal of The Electrochemical Society 162 (9) (2015) A1836–A1848. doi:10.1149/2.0551509jes.

[18] S. J. Julier, J. K. Uhlmann, New extension of the kalman filter to nonlinear systems, in: I. Kadar (Ed.), Signal Processing, Sensor Fusion, and Target Recognition VI, SPIE Proceedings, SPIE, 1997, p. 182. doi:10.1117/12.280797.

[19] M. Ecker, S. Käbitz, I. Laresgoiti, D. U. Sauer, Parameterization of a physico-chemical model of a lithium-ion battery: Ii. model validation, Journal of The Electrochemical Society 162 (9) (2015) A1849–A1857. doi:10.1149/2.0541509jes.

[20] J. Schmalstieg, C. Rahe, M. Ecker, D. U. Sauer, Full cell parameterization of a high-power lithium-ion battery for a physico-chemical model: Part i. physical and electrochemical parameters, Journal of The Electrochemical Society 165 (16) (2018) A3799–A3810. doi:10.1149/2.0321816jes.

[21] Matthias Faber, Simon Ritz, Martin Florian Börner, Dirk Uwe Sauer, Technique to determine the specific heat capacity of lithium-ion battery cells, AABC Europe 2019. doi:10.13140/RG.2.2.14632.11521.

[22] Y. Xie, S. Shi, J. Tang, H. Wu, J. Yu, Experimental and analytical study on heat generation characteristics of a lithium-ion power battery, International

Journal of Heat and Mass Transfer 122 (2018) 884–894. doi:10.1016/j.ijheatmasstransfer.2018.02.038.

[23] J. Zhang, B. Wu, Z. Li, J. Huang, Simultaneous estimation of thermal parameters for large-format laminated lithium-ion batteries, Journal of Power Sources 259 (2014) 106–116. doi:10.1016/j.jpowsour.2014.02.079.

[24] S. J. Drake, D. A. Wetz, J. K. Ostanek, S. P. Miller, J. M. Heinzel, A. Jain, Measurement of anisotropic thermophysical properties of cylindrical li-ion cells, Journal of Power Sources 252 (2014) 298–304. doi:10.1016/j.jpowsour.2013.11.107.

[25] M. Fleckenstein, S. Fischer, O. Bohlen, B. Bäker, Thermal impedance spectroscopy - a method for the thermal characterization of high power battery cells, Journal of Power Sources 223 (2013) 259–267. doi:10.1016/j.jpowsour.2012.07.144.

[26] I. D. Campbell, M. Marzook, M. Marinescu, G. J. Offer, How observable is lithium plating? differential voltage analysis to identify and quantify lithium plating following fast charging of cold lithium-ion batteries, Journal of The Electrochemical Society 166 (4) (2019) A725–A739. doi:10.1149/2.0821904jes.

[27] Springer-Verlag GmbH, VDI-Wärmeatlas, Springer Berlin Heidelberg, Berlin, Heidelberg, 2013. doi:10.1007/978-3-642-19981-3.

[28] K&K Associates, Thermal Network Modeling Handbook, K&K Associates, Westminster, 1997.

Appendix A. Simulation Parameters

As described in section 4.1, the anode diffusion coefficient was adjusted according to the more recent methodology presented in [20]. Figure A.9 depicts these changes.

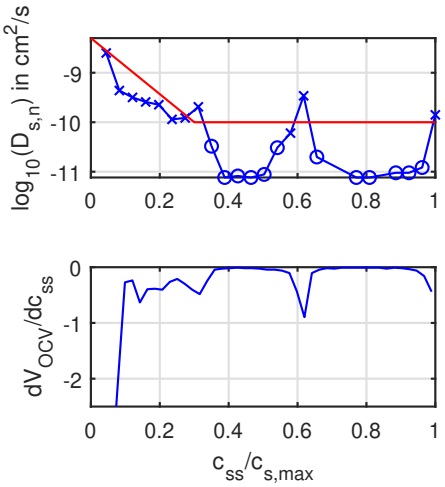

Figure A.9: Diffusion coefficient (top) and differential voltage (bottom) of an anode coin cell.

The original anode diffusion coefficient over SOC is shown in the top graph in blue. Validity of these measurements was then ensured, by evaluating the anode's OCV slope over SOC as depicted in the lower plot. Measurements are only valid, if the electrode is currently not operated in a two-phase region. This is ensured by requiring absolute value of the slope to be above a certain threshold. Valid measurements are depicted with crosses (x), invalid measurements with circles (o). The new regression function for the diffusion coefficient is depicted in red.

For the calculation of the thermal conductivity between cell and environment, we assumed a vertical plate cooled by natural convection. Convection behaviour is determined by the Grashof number, defining free convection and the Prandtl number describing material related properties. The Grashof number is defined

as

$$Gr = \frac{g \cdot \beta \cdot \Delta T \cdot l^3}{v^2} \underset{\beta=1/T}{=} \frac{g \cdot \Delta T \cdot l^3}{v^2 \cdot T} \tag{A.1}$$

with g as the gravitational constant, β as the volume expansion coefficient usually assumed as $1/T$ for ideal gases, ΔT as the temperature difference between surface and ambient, l as the plate length and v as the kinematic viscosity of air [27]. For our problem we assumed $v = 135 \cdot 10^{-7}\,\frac{\mathrm{m}^2}{\mathrm{s}}$, $\Delta T = 15\,\mathrm{K}$, $l = 0.1\,\mathrm{m}$. The Prandtl number was assumed to be $Pr \approx 0.71$ [27].

Following [28], the Grashof and Prandtl numbers can now be used to describe the heat transfer coefficient h. Since assuming a cell surface temperature of $10\,^{\circ}\mathrm{C}$ and an air temperature of $-5\,^{\circ}\mathrm{C}$ results in $10^3 < Gr \cdot \mathrm{Pr} < 10^9$, laminar flow is assumed so that

$$h = C_1 \cdot \frac{\lambda}{l} \cdot \sqrt[4]{Gr \cdot \mathrm{Pr}} \tag{A.2}$$

with $\lambda = 0.0262\,\frac{\mathrm{W}}{\mathrm{mK}}$ as the thermal conductivity and C_1 as a geometry constant which is 0.548 for a vertical short wall ($l < 60.96\,\mathrm{cm}$) with a warm wall and cool gas. For the given temperatures, the heat transfer coefficient is $h = 5.49\,\frac{\mathrm{W}}{\mathrm{m}^2\mathrm{K}}$. Since both sides are subject to convection, we doubled the value and multiplied it with the cell surface so that the cell's heat is dissipated with a rate of $0.1164\,\mathrm{W\,K^{-1}}$.

	Parameter	Unit	Cathode	Separator	Anode
d	thickness	µm	54.5	19	73.7
w	width	mm	4080	4080	4080
h	height	mm	101	101	101
ϵ	porosity		0.296	0.508	0.329
τ	tortuosity		1.94	1.67	2.03
$\sigma_{s,e}$	conductivity	$\mathrm{S\,cm^{-1}}$	0.681	see [17]	0.14
$E_{A,\sigma}$	conductivity activation energy	$\mathrm{J\,mol^{-1}}$	-	17.1e3	-
$T_{ref,\sigma}$	reference temperature	K	-	296.15	-
α	transfer coefficient		0.5	-	0.5
i_0	exchange current density @ 50 % SOC	$\mathrm{A\,cm^{-2}}$	2.23e-4	-	5.39e-4
$E_{A,i0}$	charge transfer activation energy	$\mathrm{J\,mol^{-1}}$	43.6e3	-	53.4e3
$T_{ref,i0}$	reference temperature	K	296.15	-	296.15
$c_{s,max}$	maximum lithium concentration	$\mathrm{mol\,L^{-1}}$	48.58	-	31.92
R_p	particle radius	µm	6.49	-	13.7
p	active material volume fraction		0.40832	-	0.372405
$c_{s,0}/c_{s,max}$	initial concentration		0.257886	-	0.810169
$c_{e,0}$	initial concentration	$\mathrm{mol\,L^{-1}}$	-	1	-
$D_{s,e}$	diffusion coefficient	$\mathrm{cm^2\,s^{-1}}$	see [17]	2.4e-6	see Appendix A
$E_{A,D}$	charge transfer activation energy	$\mathrm{J\,mol^{-1}}$	80.6e3	17.1e3	30.3e3
$T_{ref,D}$	reference temperature	K	296.15	296.15	296.15
t^+	Transference number		-	0.26	-
C_b	Thermal capacity bulk	$\mathrm{J\,K^{-1}}$		165	
C_c	Thermal capacity case	$\mathrm{J\,K^{-1}}$		1	
σ_{bc}	Thermal conductivity coil to case	$\mathrm{W\,m^{-1}\,K^{-1}}$		2.15	
σ_{ca}	Thermal conductivity case to ambient	$\mathrm{W\,m^{-1}\,K^{-1}}$		12	

Table A.2: Model Parameters